Measurement of the compressive crack resistance curve of composites using the size effect law

Published in:
Composites Part A: Applied Science and Manufacturing

Document Version:
Peer reviewed version

Queen's University Belfast - Research Portal:
Link to publication record in Queen's University Belfast Research Portal

Measurement of the compressive crack resistance curve of composites using the size effect law

G. Catalanotti [a,*], J. Xavier [b], P.P. Camanho [a]

[a] *DEMec, Faculdade de Engenharia, Universidade do Porto, Rua Dr. Roberto Frias, 4200-465, Porto, Portugal*
[b] *CITAB, University of Trás-os-Montes e Alto Douro, Apartado 1013, 5001-801 Vila Real, Portugal.*

Abstract

This paper presents a new methodology to measure the compressive crack resistance curve of the longitudinal plies of carbon-epoxy laminates. The methodology is based on three main steps: the first one corresponds to the determination of the energy release rate of cross-ply laminates with two edge cracks using a parametric finite element model. The energy release rate is used in the definition of a relation between the crack resistance curve and the size effect. Finally, experimental tests are performed in scaled double-edge notched specimens to quantify the size effect law, thus proving the last piece of information required to define the crack resistance curve. The full crack resistance curve is obtained for the IM7-8552 carbon epoxy composite material. The methodology proposed in this paper overcomes the inherent limitations of the existing test methods, and it serves as the basis for the identification of cohesive laws used in some analysis models.

Key words:

A. Polymer-matrix composites (PMCs), B. Fracture toughness, C. Analytical modelling, D. Mechanical testing

1 Introduction

The development of a new generation of tougher composite materials presents several challenges to the existing methods for the measurement of the fracture toughness associated with cracks that propagate perpendicularly to the fiber direction. The intra-laminar fracture toughness is relevant not only for material screening and qualification, but also to define the softening laws used in recent analysis models that predict the ultimate strength of composite structures [1–5].

The Compact Tension (CT) test specimen [6,7] is normally used to measure the fracture toughness and the crack resistance curve (R-curve) of composite materials reinforced by unidirectional fibres. While reliable results can be obtained for brittle material systems using appropriate data reduction methods [8,7], the introduction of tougher resins leads to higher loads for crack propagation, which may cause buckling of the unnotched end of the CT test specimen [9].

There is also the need to measure the fracture toughness and the corresponding R-curve associated to the propagation of a kink-band, which shows a crack-like behaviour [10–12] with an R-curve that results from the broadening of the damage height [11]. It is considered here that the compact compression test specimen is inadequate to measure the compressive crack resistance curves of polymer composite materials. In fact, the correction factor used in the data reduction method of the compact compression test method to calculate the energy release rate is the same as that used in the compact tension

* Corresponding author
  Email address: `giuseppe.catalanotti@fe.up.pt` (G. Catalanotti).

method. However, the contact tractions that occur on the crack faces during a compact compression test render the data reduction method inaccurate. This was demonstrated in a previous investigation [7] where the $\mathcal{J}$-integral around the crack tip was computed using digital image correlation. It was shown [7] that the R-curve of the compact test specimens using the $\mathcal{J}$-Integral and the data reduction method proposed by Pinho et al. [6] are virtually the same for tension but not for compression.

It should also be noted that the compact compression specimen triggers diffused damage during the propagation of the kink-band, artificially increasing the value of the measured fracture toughness, and that it is not possible to identify the location of the tip of the kink band [7]. Therefore, it is considered that while the compact compression test method may be used to measure the initial value of the fracture toughness it does not provide reliable information for the generation of the R-curve.

This means that the analysts have no reliable test methods to measure some of the required material properties, namely the fracture toughness related with the propagation of a kink-band and the corresponding R-curve.

This fact provides the motivation for this paper, whose objective is to propose a new methodology to obtain the R-curve of composite materials that fail by the propagation of a kink-band. The approach proposed is based on the relation between the size effect law and the R-curve, and it will be presented in the following order: section 2 describes the analytical model that relates the size effect law obtained in cross-ply laminates with two edge notched to the R-curve. Section 3 presents the details of the compression tests performed in the double-edge notched specimens manufactured using IM7-8552 carbon-epoxy. Section 4 combines the analytical model and the test results to fully

3

50   define the R-curve for the material under investigation, and Section 5 presents

51   the main conclusions of the paper.

52   ## 2   Analytical Model

53   Consider the geometry shown in Figure 1. The width is equal to $2w$, the length

54   is $3w$, and a_0 is the initial crack length.

55   [Fig. 1 about here.]

56   In a two-dimensional orthotropic body, considering x and y as the preferred

57   axes of the material, the energy release rate (ERR) in mode I for a crack

58   propagating in the x-direction reads [13]:

$$\mathcal{G}_I = \left(s_{11} s_{22} \frac{1+\rho}{2} \right)^{1/2} \lambda^{-1/4} \mathcal{K}_I^2 \tag{1}$$

59   where s_{lm} are the components of the compliance matrix computed in the x-

60   y coordinate system, $\mathcal{K}_I$ is the stress intensity factor, and λ, ρ are the two

61   dimensionless elastic parameters defined as:

$$\lambda = \frac{s_{11}}{s_{22}}, \qquad \rho = \frac{2\,s_{12} + s_{66}}{2\,\sqrt{s_{11} s_{22}}} \tag{2}$$

62   Suppose that the crack is propagating in a $[0/90]_{ns}$ cross-ply laminate. In this

63   case, $s_{11} = s_{22}$, $\lambda = 1$ and equation (1) reads:

$$\mathcal{G}_I = \frac{1}{E} \sqrt{\frac{1+\rho}{2}} \mathcal{K}_I^2 \tag{3}$$

4

64 where E is the laminate Young's modulus along the x (or y) direction.

65 The stress intensity factor of the double edge notched specimen shown in
66 Figure 1 is a function of ρ, of the remote stress σ, and of the shape and the
67 size of the specimen:

$$\mathcal{K}_I = \sigma \sqrt{w} \sqrt{\phi(\alpha, \rho)} \tag{4}$$

68 where $\alpha = a/w$ is the shape-parameter and $\phi(\alpha, \rho)$ is the correction factor
69 for the geometry and orthotropy of the material. Substituting (4) in (3) the
70 energy release rate reads:

$$\mathcal{G}_I = \frac{1}{E} \sqrt{\frac{1+\rho}{2}} \, \sigma^2 \, w \, \phi(\alpha, \rho) = \frac{1}{4wE} \sqrt{\frac{1+\rho}{2}} \left(\frac{P}{t}\right)^2 \phi(\alpha, \rho) \tag{5}$$

71 where t is the thickness of the specimen.

72 Following the approach proposed in [7] the dimensionless function $\phi(\alpha, \rho)$
73 can be defined for the problem under consideration using the Finite Element
74 Method (FEM). For this purpose a parametric Finite Element model was cre-
75 ated using Python [14] together with Abaqus 6.8-3 Finite Element code [15].

76 In this model the characteristic distance w is taken constant and equal to the
77 unity, while the variables are: i) the shape parameter or, in other words, the
78 crack length $0 < \alpha < 1$; ii) the dimensionless parameter ρ that takes into
79 account the effect of the orthotropy of the material ($0 \leq \rho \leq 20$). There is no
80 need to take into account λ because for the layup that was chosen (balanced
81 cross ply) its value is constant and equal to one; therefore λ is not accounted
82 for in the calibration of the model. Figure 2 shows the mesh of the finite

5

83 element model used to define the function ϕ.

84   [Fig. 2 about here.]

85 Taking advantage of the symmetry of the problem, only one quarter of the

86 specimen was modeled. The 4-node quadratic, reduced integration element,

87 CPS4R, is used.

88 The displacement u_y is applied on the top face of the model and represents

89 the loading condition that will be used in the experiments. The nodes on the

90 top faces are free to move in x direction; this means that a frictionless con-

91 tact occurs between the specimen and the loading system. The Virtual Crack

92 Closure Technique (VCCT) [16] is used to compute the energy release rate at

93 the crack tip, $\mathcal{G}_I$. The applied load P is calculated summing the reactions at

94 the nodes.

Using the results obtained in the FE analysis the correction factor ϕ is ap-

proximated by the following polynomial:

$$\phi\left(\alpha,\rho\right) = \frac{\alpha}{1-\alpha} \sum_{i=1}^{M} \sum_{j=1}^{N} \Phi_{ij} \, \rho^{j-1} \, \alpha^{i-1} \tag{6}$$

95 where Φ_{ij} is the element of the matrix $\boldsymbol{\Phi}$ at the row i and at the column j,

96 and M and N are the number of rows and columns of $\boldsymbol{\Phi}$ respectively. The

97 matrix $\boldsymbol{\Phi}$ reads:

6

$$\boldsymbol{\Phi} = \begin{bmatrix} 4.315050777 & -0.1833177904 & 0.01642021976 & -4.829962430\text{E-}4 \\ -5.148136502 & -0.3554678337 & -9.974634025\text{E-}4 & 4.975387379\text{E-}4 \\ 2.385888075 & 1.339974300 & -0.05966399650 & 7.544565390\text{E-}4 \\ -0.2810124370 & -0.8040552990 & 0.04491874691 & -7.869467548\text{E-}4 \end{bmatrix} \quad (7)$$

Figure 3 shows the numerical points obtained in the FE simulations (each point corresponds to one simulation) and the surface fitting function of equation (6).

[Fig. 3 about here.]

Figure 4 shows the relation between ϕ and α for different values of the dimensionless elastic parameter ρ obtained by the polynomial approximation and by the FE model. It can be noticed that the fitting obtained is excellent. The curve with $\rho = 1$ corresponds to the isotropic case. The close range $\rho \in [0, 20]$ should cover all the practical applications. For example for a IM7-8552 $[0/90]_{ns}$ laminate ($E_1 = 171420\text{MPa}$, $E_2 = 9080\text{MPa}$, $G_{12} = 5290\text{MPa}$, $\nu_{12} = 0.32$) the elastic parameters calculated using the classical lamination theory are $E_x = E_y = 90648\text{MPa}$, $G_{xy} = 5290\text{MPa}$, $\nu_{xy} = \nu_{xy} = 0.032$ and, from (2), $\rho = 8.54$.

[Fig. 4 about here.]

After defining ϕ, it is observed that the energy release rate $\mathcal{G}(a)$ is an increasing function of the crack length, or, in other words, the proposed specimen has a *positive geometry* [17]. Equation (5) can be re-written as:

7

$$\mathcal{G}_I\left(a+\Delta a\right)=\frac{1}{4wE}\sqrt{\frac{1+\rho}{2}}\left(\frac{P}{t}\right)^2\phi\left(\alpha_0+\frac{\Delta a}{w},\rho\right) \tag{8}$$

where $\alpha_0=a_0/w$ (see Fig. 1). The energy release rate $\mathcal{G}_I\left(a+\Delta a\right)$ and the schematic representation of the R-curve of the material $\mathcal{R}_I\left(\Delta a\right)$ are shown in Fig. 5. The dotted line represents the $\mathcal{G}_I\left(a+\Delta a\right)$ at a constant load P. The crack cannot propagate at a constant load if $\mathcal{G}_I<\mathcal{R}$ while it will propagate dynamically if $\mathcal{G}_I>\mathcal{R}$. The dashed line in Fig. 1, tangent at the R-curve, represents the crack-driving force at the peak load, P_u (or at the maximum remote stress, σ_u).

[Fig. 5 about here.]

In summary, for different sizes w_k the driving-force curves $\mathcal{G}_I$ corresponding at the peak loads P_{uk} are tangent to R-curve, $\mathcal{R}$. This fact will be used to measure the R-curve.

2.1   Obtaining the R-curve from size effect

Based on the previous observations, the peak load, P_u, or the ultimate nominal stress, $\sigma_u=P_u/\left(2wt\right)$, can be obtained from the following system of equations:

$$\begin{cases} \mathcal{G}_I\left(a+\Delta a\right)=\mathcal{R}\left(\Delta a\right) \\[2mm] \frac{\partial\mathcal{G}_I(a+\Delta a)}{\partial\Delta a}=\frac{\partial\mathcal{R}(\Delta a)}{\partial\Delta a} \end{cases} \tag{9}$$

Assuming that the size effect law, $\sigma_u=\sigma_u\left(w\right)$, is known, substituting (5) in the first of equations (9) yields:

8

$$\frac{1}{E}\sqrt{\frac{1+\rho}{2}}\,\sigma_u^2\,w\,\phi\left(\alpha_0 + \frac{\Delta a}{w}\right) = \mathcal{R}\left(\Delta a\right) \qquad (10)$$

131   This equation holds for every w. Following [17], differentiating (10) with re-

132   spect to w, under the hypothesis that geometrically similar specimens are

133   tested (α_0 is not a function of w) and remembering that, by definition, the

134   R-curve does not depend on the size of the specimen w ($\partial \mathcal{R}/\partial w = 0$), results

135   in:

$$\frac{1}{E}\sqrt{\frac{1+\rho}{2}}\,\frac{\partial}{\partial w}\left(\sigma_u^2\,w\,\phi\left(\alpha_0 + \frac{\Delta a}{w}\right)\right) = 0 \qquad (11)$$

136   The R-curve, $\mathcal{R}\left(\Delta a\right)$, can be obtained solving (11) for $w = w\left(\Delta a\right)$, and by

137   replacing this solution in equation (10).

138   The proposed method provides the R-curve of the laminate. The R-curve of

139   the 0° plies is obtaining neglecting the fracture toughness of the 90° plies, as

140   previously proposed by Pinho [6]. The energy balance for self-similar crack

141   propagation da reads:

$$\mathcal{R}\,h\,\mathrm{d}a = \mathcal{R}_0\,h_0\,\mathrm{d}a + \mathcal{R}_{90}\,h_{90}\,\mathrm{d}a \qquad (12)$$

142   where $\mathcal{R}_0$ and $\mathcal{R}_{90}$ are the R-curves for the 0° and 90° plies respectively while

143   h, h_0 and h_{90} are respectively the thickness of the laminate, of the 0° and of

144   the 90° plies respectively. Taking into account that $\mathcal{R}_{90} << \mathcal{R}_0$, and $h_0 =$

145    $h_{90} = h/2$, equation (12) results in:

$$\mathcal{R}_0 = 2\,\mathcal{R} \qquad (13)$$

146 Therefore the fracture toughness in longitudinal direction $\mathcal{R}_0$ is simply obtained

147 tained as twice the value of the fracture toughness of the laminate $\mathcal{R}$.

3 Experiments

3.1 Material and specimen configurations

150 The material used is the Hexcel IM7-8552 carbon fiber reinforced epoxy. The

151 elastic properties of the material were previously obtained in [18] and are

152 shown in Table 1, where E_1 and E_2 are the longitudinal and the transverse

153 Young's modulus respectively, G_{12} is the shear modulus, and ν_{12} is the major

154 Poisson's ratio.

155 [Table 1 about here.]

156 The $[0/90]_{8s}$ layup with a nominal thickness of 4mm is used. The laminate was

157 cured in a hot–press according to the manufacturer's specifications. The curing

158 cycle consists of three different stages: i) keeping the laminate at 110°C for 1

159 hour; ii) increasing the temperature up to 180°C and keeping this temperature

160 for 2 hours iii) cooling at 3°C/min. The pressure of 7 bar was used during all

161 the curing cycle.

162 After curing, the laminate was cut using a diamond saw disk to the nominal

163 specimens size and the notches were machined using a vertical mill equipped

164 with 1mm diameter drill bit.

165 Six sizes were chosen for the specimens, corresponding to the references A to

166 F. The nominal dimensions of the specimens are shown in Figure 6. Three

167 specimens were tested for each specimen type. It should be noticed that the

10

168 initial crack length a_0 was chosen to be one-half of the characteristic length

169 for all specimens. Therefore the parameter α_0 is equal to 0.5.

170 [Fig. 6 about here.]

171 The specimens manufactured are scaled from the specimen shown in Figure 1.

172 It should be noted that in the actual specimen the crack faces are separated

173 by a finite distance of 1mm. This ensures that there is no contact of the crack

174 faces; such contact would have invalidated the experimental results. It should

175 also be noted that the shape of the crack tip (semicircular, 1mm of diameter)

176 does not have an influence on the correct determination of the R-curve of the

177 material because: i) the crack tip shape does not influence the value of the

178 fracture toughness in compression [19], and ii) after the initial propagation

179 the crack tip can be considered *sharp* and this should not influence the value

180 of the fracture toughness at unstable crack propagation.

181 After manufacturing, the specimens were painted with a matte white. After

182 drying the specimens, a speckle was made for all the specimens with the help

183 of an airbrush (see Fig. 7).

184 [Fig. 7 about here.]

185 *3.2 Photo-mechanical compression tests*

186 The compression tests were performed with the support of the digital image

187 correlation (DIC) system (Fig. 8). The tests were carried out on a Instron

188 4208 universal testing machine under displacement control, with a cross-head

189 displacement rate of 0.1 mm/min and at room temperature of 22°C and rel-

190 ative humidity of 56%. The load was measured using a 100 kN load cell. The

11

191 Spider data acquisition system along with Catman software was used to record
192 the strain gauge signal (in the specimens equipped with a strain gauge). 350
193 Ω strain gauges from Vishay Micro-Measurement, C2A-06-062LW-350, were
194 used to verify if buckling occurs in the longest specimens (F specimens). To
195 replicate the same frictionless condition imposed numerically for the calcula-
196 tion of the correction factor ϕ, a thin layer of molybdenum disulfide (MoS2)
197 was used between the specimen and the loading system. The self alignment
198 system shown in Figure 8(b) was also used. The system consists of two parts
199 connected by a spherical joint. The upper part of the self alignment system is
200 in contact with the specimen and it is equipped with a tungsten-carbide insert
201 to prevent indentation; the bottom part is bolted to the frame of the testing
202 machine. By allowing small rotations between the two parts, the self alignment
203 device avoids premature failure of the specimen that may result from possible
204 parallelism errors between the two faces in contact with the loading system.

205 [Fig. 8 about here.]

206 At the scale of observation used in this work, the textured pattern required for
207 the digital image correlation was created across the gauge section by means of
208 aerosol and airbrush painting, as shown in Fig. 9. The Aramis DIC-2D v6.0.2-
209 6 system was used in this work [20,21]. An 8-bit Baumer Optronic FWX20
210 camera coupled with a Nikon AF Micro-Nikkor 200 mm f/4D IF-ED lens were
211 used for image acquisition. The optical devices and measuring parameters are
212 summarised in Table 2 for each specimen configuration (see also Fig 7).

213 [Fig. 9 about here.]

214 A subset size and a subset step of 15×15 pixel^2 and 13×13 pixel^2 were chosen,
215 respectively (Table 2). In order to guarantee a suitable speckle pattern for this

12

216 virtual gauge an airbrush was used (Iwata Custom 181 Micron CM-B model
217 with a fluid nozzle of 0.18 mm in diameter and spray 182 range lower than
218 60 microns). With this marking technique the accurate uniformity, isotropy
219 and spot size can be achieved. A slightly overlapping of 2 pixels between ad-
220 jacent subsets was chosen in order to enhance spatial resolution in the strain
221 reconstruction. A strain base length of 5 subsets was selected for strain com-
222 putation. The displacement and strain resolution of the measured is expected
223 in the range of 2×10^{-2} pixel and 0.02-0.04% respectively (Table 2).

224 [Table 2 about here.]

225 *3.3   Experimental results*

226 Representative load vs. displacement curves are shown in Figure 10 for the
227 different specimens.

228 [Fig. 10 about here.]

229 The F specimens (the longest specimens) were equipped with a strain gauge
230 on the back side of the specimen (the side without the speckle for the DIC).
231 The strain measured by the strain gauge was compared to the strain measured
232 by the DIC (virtual strain gauge) on the front side in the location correspond-
233 ing to the physical strain gauge. The strain of the virtual strain gauge was
234 obtained as the average of the longitudinal strain on the rectangular region
235 symmetric to the strain gauge and with the dimension of the electrical grid of
236 the physical strain gauge. Figure 11 shows the comparison between the signal
237 of the physical and of the virtual strain gauge for a representative specimen
238 and the location of the strain gauge in the specimen. As virtually there are no

13

239 differences, it is concluded that no buckling occurred in the test specimens.

240 [Fig. 11 about here.]

241 The digital image correlation can be used to further verify the validity of the

242 tests performed. Figure 12 shows the contour plot of the shear strain, γ_{xy}. The

243 perfect antisymmetry of the strain field with respect to the longitudinal axis

244 of the specimen and the zero value of the shear strain all over the central part

245 of the specimen (and in particular near the crack tip) shows that the loading

246 system used is appropriate. Any misalignment would result in a different field

247 of the shear strain, and mixed mode crack propagation would have occurred.

248 [Fig. 12 about here.]

249 The fracture surface for the two types of specimens (A and F) are shown

250 in Figure 13. It is observed in both specimens that the compressive fracture

251 occurred along the direction of the initial notches.

252 [Fig. 13 about here.]

253 The summary of the results is shown in Table 3. For each type of specimen

254 the characteristic size w, the peak load P_u, and the standard deviation are re-

255 ported. The results obtained are used in the following section in the calculation

256 of the R-curve.

257 [Table 3 about here.]

14

4   Obtaining the R-curve from size effect

As previously explained, the use of the size effect method to obtain the R-curve of the material requires the knowledge of the size-effect law $\sigma_u = \sigma_u(w)$ that relates the nominal remote stress to the characteristic size of the body. According to Bažant and Planas [17] different kind of regression plots can be used to find the size-effect laws: i) bilogarithmic plot ($\ln \sigma_u$ vs. $\ln w$); ii) linear regression I (σ^{-2} vs. w); iii) linear regression II (($\sigma w)^{-2}$ vs. $1/w$); iv) inverse bilogaritmic plot ($\ln w$ vs. $\ln \sigma_u$). Those methods yield approximatively the same results.

After the inspection of the data obtained experimentally and reported in Table 3, the linear regression I was selected. Figure 14 shows σ^{-2} as a function of the characteristic size w. The experimental points and the linear fitting are also reported.

[Fig. 14 about here.]

The size effect law of the material can be expressed as:

$$\sigma_u = (m\,w + q)^{-\frac{1}{2}} \tag{14}$$

where m and q are the slope and the intercept of the linear fit respectively. It should be noted that the linear fit was obtained with a coefficient of determination of $R^2 = 0.92$.

Knowing the size effect law, equation (11) can be solved for $w = w(\Delta a)$. All the other parameters are known: $\alpha_0 = 0.5$, $E = 90648$MPa, and $\rho = 8.54$. Substituting $w = w(\Delta a)$ in equation (10) enables the calculation of the R-

15

278 curve of the laminate, $\mathcal{R}$. Finally $\mathcal{R}_0$ is obtained by multiplying by two the

279 value of $\mathcal{R}$ for every (Δa).

280 Figure 15 shows the $\mathcal{R}_0$ obtained using this methodology as the envelope of the

281 crack driving force curves. The value of the steady-state value of the fracture

282 toughness can be obtained as:

$$\mathcal{R}_{ss} = \lim_{w \to \infty} \mathcal{R}_0 = \frac{\sqrt{2(1+\rho)}}{E} \frac{\phi_0}{m} = 61 \text{kJ/m}^2 \tag{15}$$

283 where $\phi_0 = \phi|_{\alpha=\alpha_0}$. It is interesting to note that the value of the fracture tough-

284 ness previously measured using the compact compression test specimens [7],

285 47.5kJ/m^2, corresponds to just one point in the rising R-curve.

The length of fracture process zone reads [17]:

$$l_{fpz} = \frac{f_0}{2 f_0'} w_0 \tag{16}$$

286 where $f_0 = \sqrt{\phi}\big|_{\alpha=\alpha_0}$, $f_0' = \partial\sqrt{\phi}/\partial\alpha\big|_{\alpha=\alpha_0}$ and w_0 is the constant of Bažant size-

287 effect law with the dimension of a length. For the linear regression used [17]

288 $w_0 = q/m$; therefore equation (16) reads:

$$l_{fpz} = \frac{f_0}{2 f_0'} \frac{q}{m} = 1.43 \text{mm} \tag{17}$$

289   [Fig. 15 about here.]

290 To simplify the use of the R-curve it is necessary to express it in an analytical

291 form that fits the points obtained by solving equations (10) and (11). The

292 following expression can be used [17]:

16

$$\begin{cases} \mathcal{R}_0 = \mathcal{R}_{ss}\left[1 - (1 - \kappa\Delta a)^n\right] & \text{if } \Delta a < l_{FPZ} \\ \mathcal{R}_0 = \mathcal{R}_{ss} & \text{if } \Delta a \geq l_{FPZ} \end{cases} \tag{18}$$

By optimal fitting the following values are obtained: $\kappa = 0.5126$ and $n = 4.289$. Figure 16 shows the analytical fitting of the R-curve.

[Fig. 16 about here.]

5 Conclusion

This paper demonstrates that it is possible to obtain the compressive R-curve of the longitudinal plies of carbon-epoxy laminates by quantifying the size effect law observed in compressive tests of scaled specimens with two edge cracks. The limiting factors of the previously proposed compact compression test method, such as the difficulty in predicting the exact location of the extremity of the kink band, do not play any role in the model developed in this paper.

Using both electrical strain gauges and the digital image correlation system it is demonstrated that the test method and specimens' geometry proposed do not result in premature buckling failure. In addition, the strain field measured by digital image correlation system indicates that the specimens are properly aligned. Therefore, the peak loads measured in the tests can be confidently used for the definition of the size effect law.

While the previous tests methods are only able to provide one single value for the compressive fracture toughness, the proposed method enables the identification of the full R-curve. The steady-state value of the fracture toughness

17

313 of the IM7-8552 carbon-epoxy composite material is $61kJ/m^2$, corresponding
314 to a length of the fracture process zone of 1.43mm.

315 The work presented in this paper can be used as the basis for material screen-
316 ing and selection, to identify cohesive laws used in the recent analysis models,
317 and to estimate the fracture toughness of multidirectional laminates using the
318 fracture toughness of the 0° plies.

Acknowledgements

References

327 [1] Vogler M, Rolfes R, Camanho PP. Modeling the inelastic deformation and
328   fracture of polymer composites part I: Plasticity model. Mechanics of Materials,
329   59(0):50 − 64, 2013.

330 [2] Camanho PP, Bessa MA, Catalanotti G, Vogler G, Rolfes R. Modeling the
331   inelastic deformation and fracture of polymer composites part II: Smeared
332   crack model. Mechanics of Materials, 59(0):36 − 49, 2013.

333 [3] Lapczyk I, Hurtado JA. Progressive damage modeling in fiber-reinforced

334 materials. Composites Part A: Applied Science and Manufacturing, 38(11):2333

335 – 2341, 2007.

336 [4] Donadon MV, Iannucci L, Falzon BG, Hodgkinson JM, de Almeida SFM. A

337 progressive failure model for composite laminates subjected to low velocity

338 impact damage. Computers & Structures, 86(11–12):1232 – 1252, 2008.

339 [5] Raimondo L, Iannucci L, Robinson P, Curtis PT. A progressive failure model

340 for mesh-size-independent FE analysis of composite laminates subject to low-

341 velocity impact damage. Composites Science and Technology, 72(5):624 – 632,

342 2012.

343 [6] Pinho ST, Robinson P, Iannucci L. Fracture toughness of the tensile and

344 compressive fibre failure modes in laminated composites. Composites Science

345 and Technology, 66:2069–2079, 2006.

346 [7] Catalanotti G, Camanho PP, Xavier J, Dávila CG, Marques AT. Measurement

347 of resistance curves in the longitudinal failure of composites using digital image

348 correlation. Composites Science and Technology, 70(13):1986 – 1993, 2010.

349 [8] Laffan MJ, Pinho ST, Robinson P, McMillan AJ. Translaminar fracture

350 toughness testing of composites: A review. Polymer Testing, 31(3):481 – 489,

351 2012.

352 [9] Blanco N, Pinho ST, Robinson P. Design and analysis of a compact tension

353 (CT) specimen for intralaminar fracture toughness characterisation of woven

354 composite laminates. In ECCM 13, 13th European Conference on Composite

355 Materials, Stockholm, June 2 - 5, 2008.

356 [10] Bažant ZP, Kim J-JH, Daniel IM, Becq-Giraudon E, ZI G. Size effect on

357 compression strength of fiber composites failing by kink band propagation. Int.

358 J. Fracture, 95:103–141, 1999.

359 [11] Moran PM, Liu XH, Shih CF. Kink band formation and band broadening in

19

360   fiber composites under compressive loading. Acta Metallurgica et Materialia,

361   43(8):2943 – 2958, 1995.

362 [12] Fleck NA, Sutcliffe MPF, Sivanshanker S, Xin XJ. Compressive failure

363   of composites due to microbuckle growth. European Journal of Mechanics

364   A/Solids, 16:65–82, 1997.

365 [13] Suo Z, Bao G, Fan B, Wang TC. Orthotropy rescaling and implications for

366   fracture in composites. Int. J. Solids and Structures, 28:235–248, 1990.

367 [14] Lutz M. Learning Python. O'Reilly Media, Inc., 3rd edition, 2008.

368 [15] Dassault Systèmes. Abaqus Version 6.8–3 Documentation, 2008.

369 [16] Krueger R. The virtual crack closure technique: History, approach and

370   applications. Technical Report NASA/CR-2002-211628 ICASE Report No.

371   2002-10, ICASE, Hampton, Virginia, April 2002.

372 [17] Bažant ZP, Planas J. Fracture and Size Effect in Concrete and Other

373   Quasibrittle Materials. CRC Press LLC, 1997.

374 [18] Camanho PP, Maimí P, Dávila CG. Prediction of size effects in notched

375   laminates using continuum damage mechanics. Composites Science and

376   Technology, 67(13):2715–2727, 2007.

377 [19] Jackson WC, Ratcliffe JG. Measurement of fracture energy for kink-band

378   growth in sandwich specimens. In Proceedings of the 2nd international

379   conference on composites testing and model identification, Comptest 2004,

380   University of Bristol, Bristol, U.K., 2004.

381 [20] Xavier J, de Jesus A, Morais J, Pinto J. Stereovision measurements on

382   evaluating the modulus of elasticity of wood by compression tests parallel to

383   the grain. Construction and Building Materials, 26:207–215, 2012.

384 [21] GOM (www.gom.com). ARAMIS, User Manual - Software - v6.0.2-6, 2009.

20

List of Figures

Fig. 1. Double edge notched compression specimen.
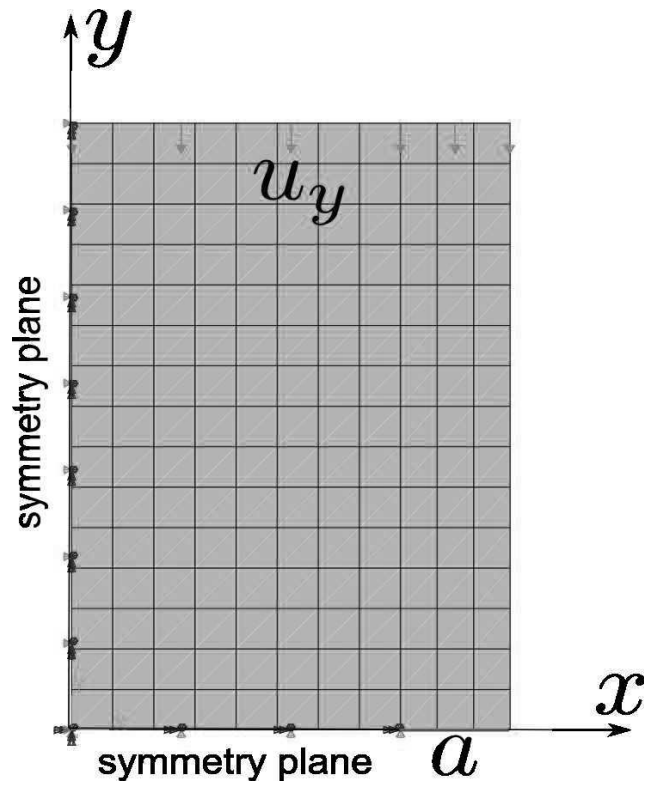
Fig. 2. Finite element model of the specimen.
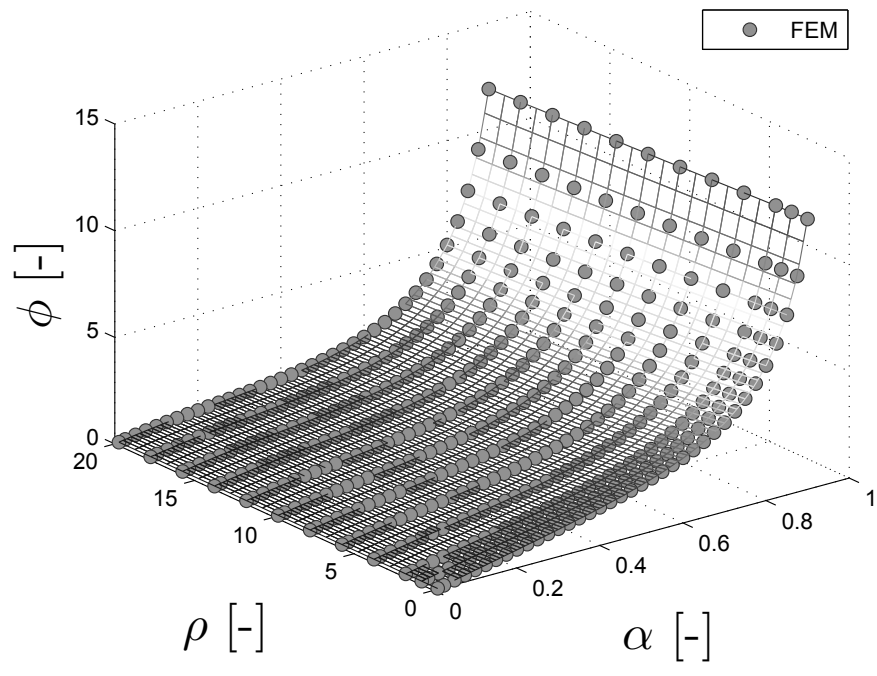
Fig. 3. Relation between ϕ and α for different values of ρ.
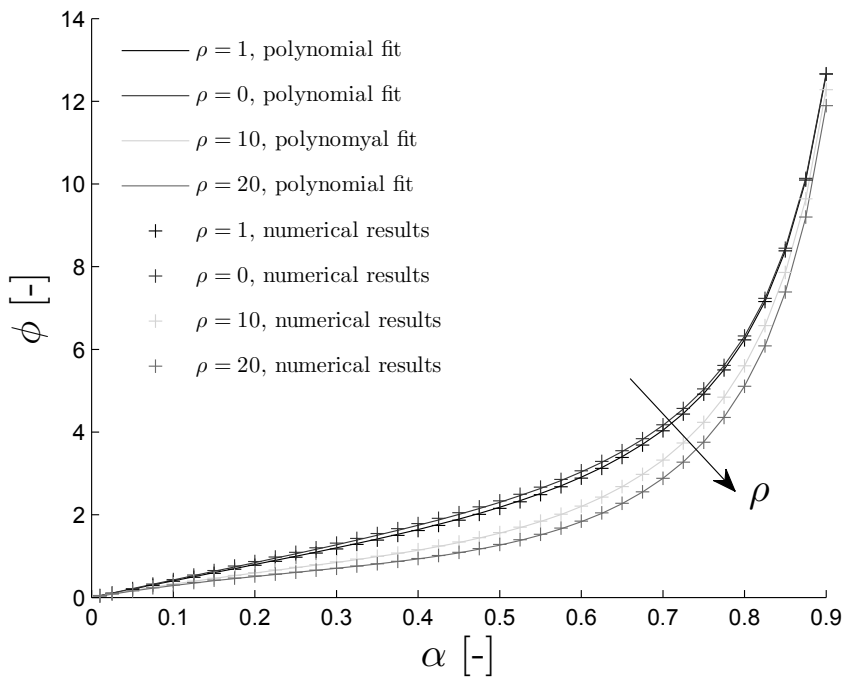
Fig. 4. Numerical points and ϕ for different values of ρ.
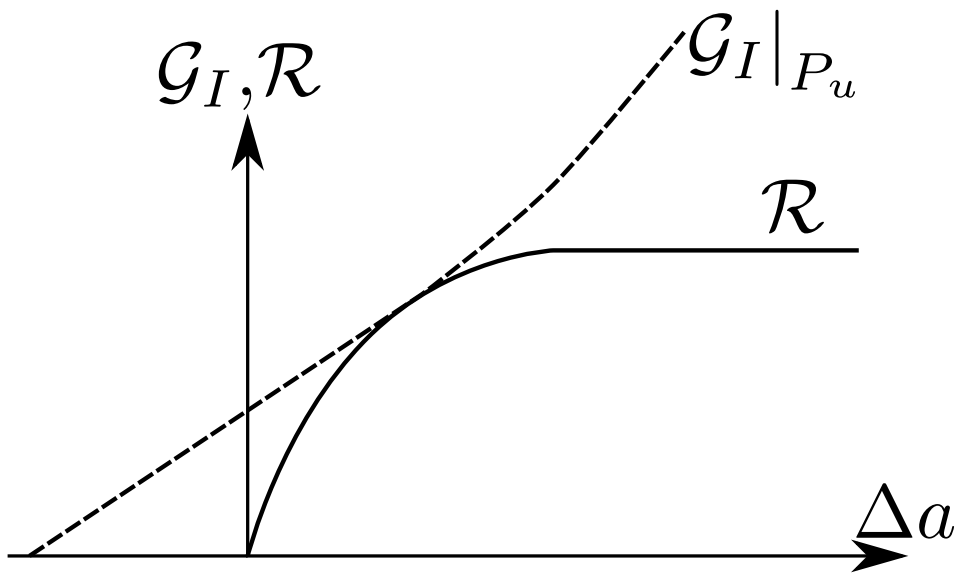
Fig. 5. Crack driving force and resistance curves.
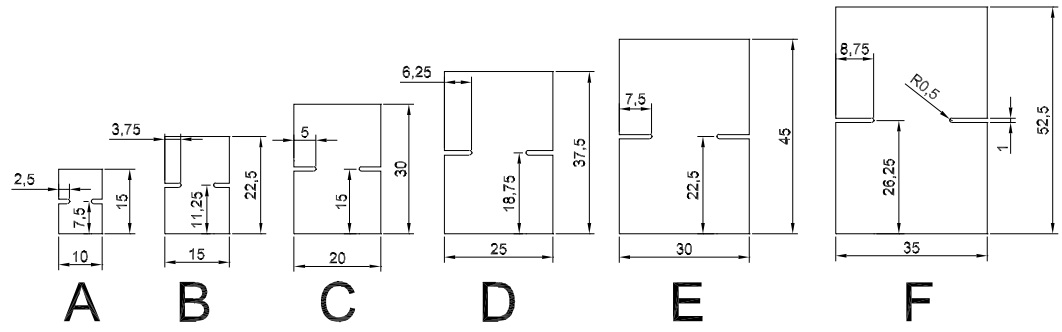
Fig. 6. Specimens' geometry (dimensions in mm).
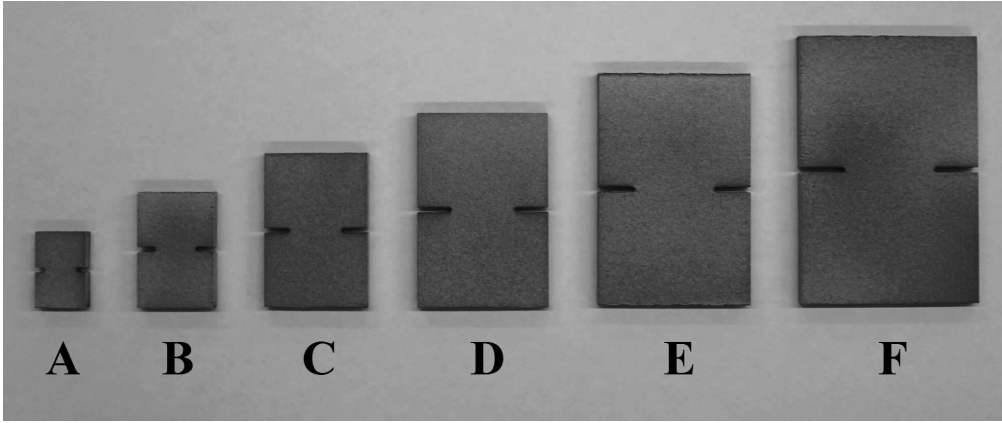
Fig. 7. Specimens' configuration.

(a) Optical set-up   (b) Loading system
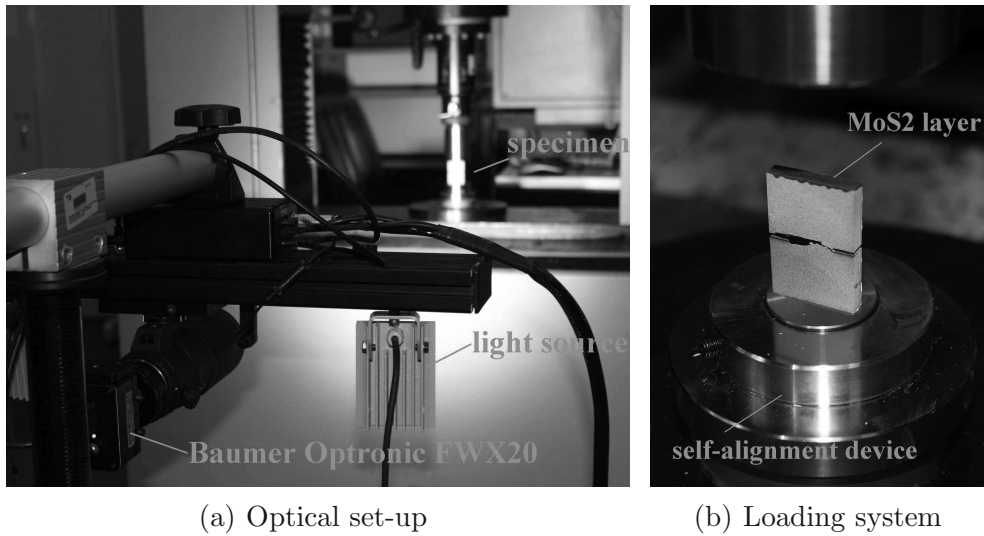
Fig. 8. Photomechanical set-up.
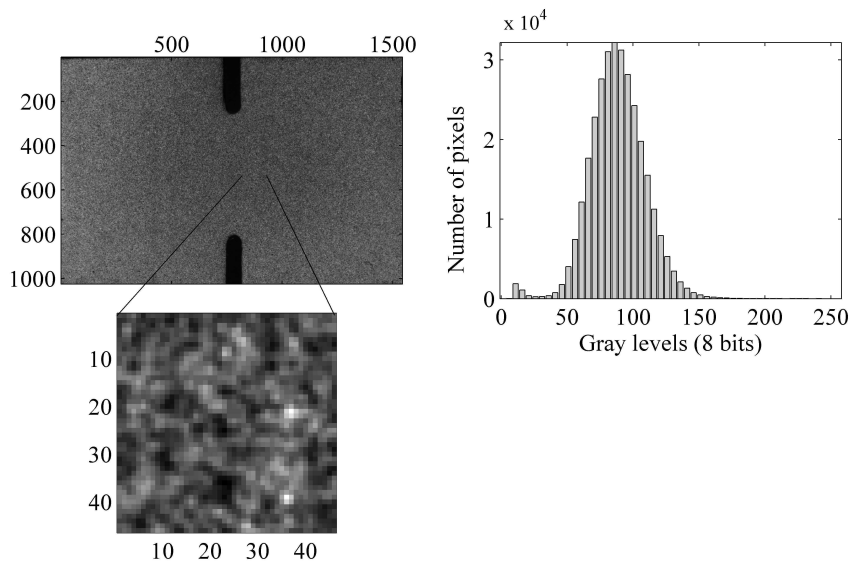
Fig. 9. Speckle pattern typically used in the digital image correlation measurements (region of interest of $1543{\times}1025$ pixel^2 ($22.0{\times}14.6$ mm^2)).
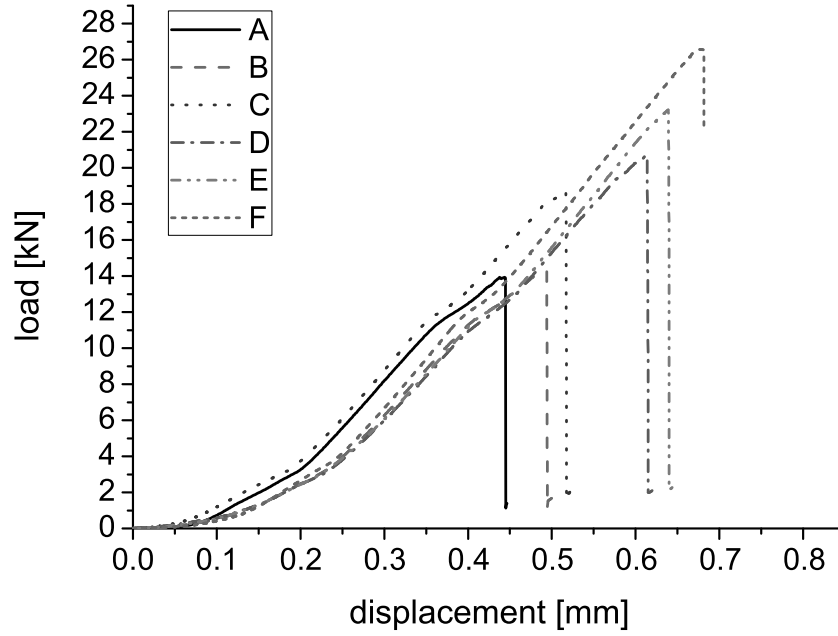
Fig. 10. Typical load displacement curves for the specimens A, B, C, D and F.
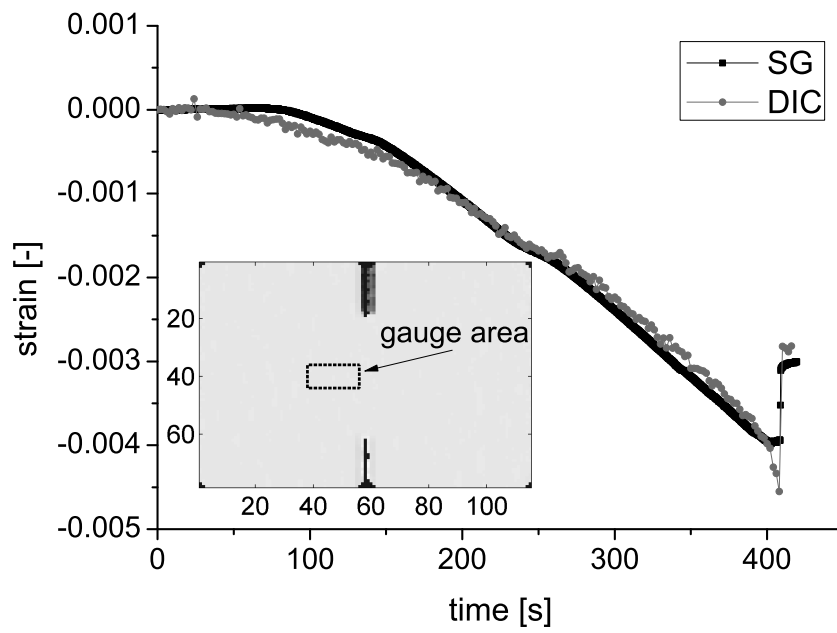
Fig. 11. Comparison between the signal of the physical (SG) and virtual (DIC) strain gauge.
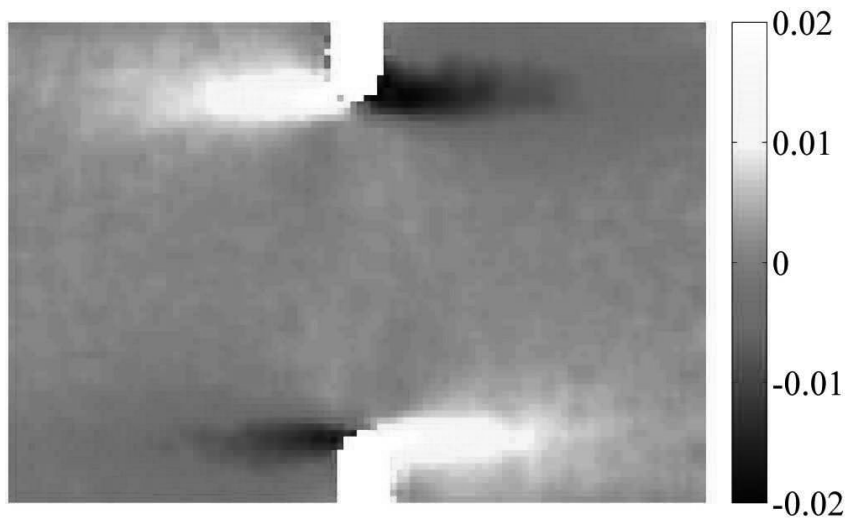
Fig. 12. Typical contour plot of the shear strain, γ_{xy}.

(a) type A   (b) type F

Fig. 13. Tested specimens (not at scale).

Equation	y=mx+q		
Adj. R-Squ	0.89741		
		Value	Standard Error
q	Intercept	5.86794E-6	2.29686E-6
m	Slope	1.27673E-6	1.90881E-7

experiments
linear fit
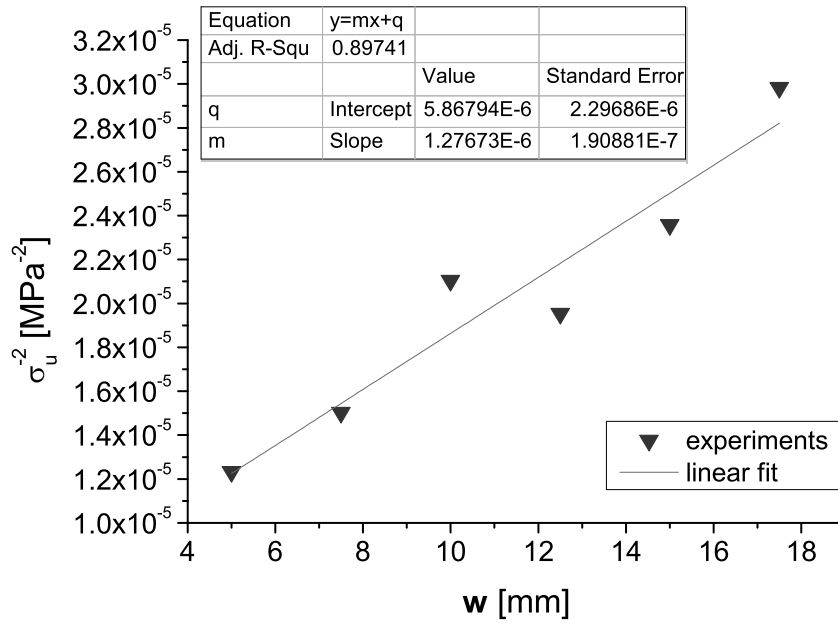
Fig. 14. σ_u^{-2} vs. w and linear fitting.
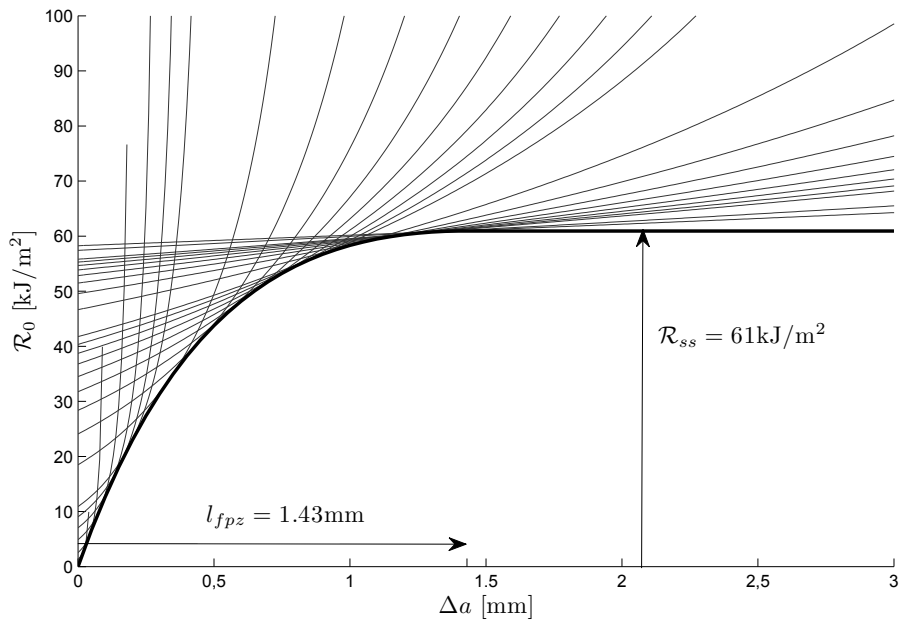
Fig. 15. Envelope of driving force curves and R-curve.

$$\mathcal{R}_0 = \mathcal{R}_{ss} \left[1 - (1 - \kappa \Delta a)^n\right]$$
$$\kappa = 0.5126, \; n = 4.298$$

Fig. 16. Analytical fitting of the R-curve.

List of Tables

E_1 [MPa]	E_2 [MPa]	G_{12} [MPa]	ν_{12}
171420	9080	5290	0.32
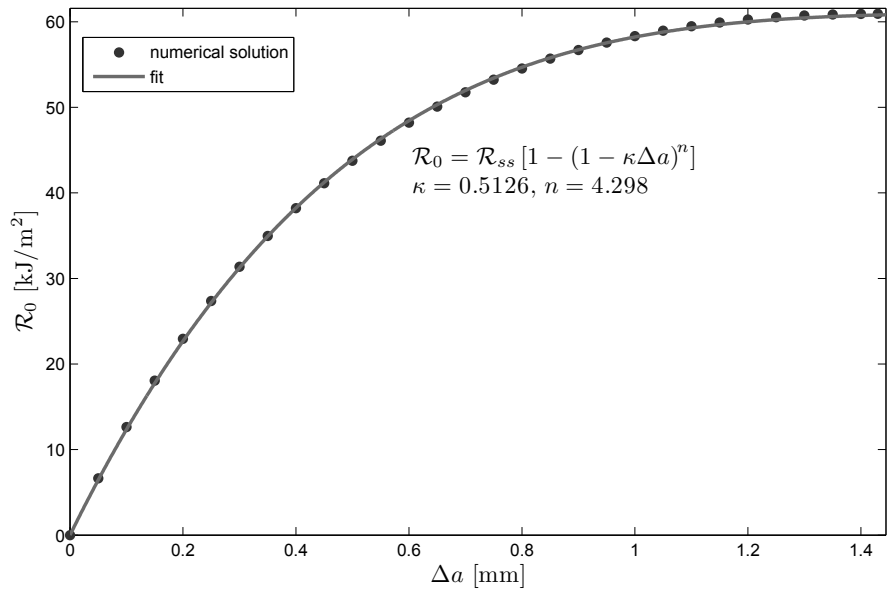
Table 1
Elastic properties of IM7-8552.

Table 2
Optical system components and measurement parameters (see Fig. 7 for A, B, C, D, E and F specimen configuration).

Camera-lens optical system						
CCD camera	Baumer Optronic FWX20					
	(8 bit, 1624×1236 pixels)					
Lens	Nikon AF Micro-Nikkor 200 mm f/4D IF-ED					
	(Working F-number: 11)					
Lighting system	LED RAYLUX 25					
Image recording	A	B	C	D	E	F
Field Of View						
(mm^2)	15.2×11.5	23.2×17.7	31.2×23.7	38.8×29.5	46.2×35.1	55.3×42.1
Working Distance						
(mm)	560	750	1000	1250	1420	1690
Conversion factor						
(mm/pixel)	0.0093	0.0143	0.0192	0.0239	0.0284	0.034
Acquisition frequency						
(Hz)	1	1	1	0.5	0.5	0.5
Exposure time (ms)	4	4	7	7	12	20
DIC (Aramis) parameters						
Subset size	15×15 pixels^2					
Subset step	13×13 pixels^2					
Strain base length	5×5 subsets					
DIC resolution						
Displacement	2×10^{-2} pixel					
Strain	0.02-0.04%					

specimen label	A	B	C	D	E	F
w [mm]	5	7.5	10	12.5	15	17.5
P_u [N]	11390	15477	17436	22622	24706	25628
STDV(P_u) [N]	2262	1421	3268	1793	1827	1028
σ_u [MPa]	285	258	218	226	206	183

Table 3
Summary of the experimental results.